

# Rate Prediction for Homogeneous Nucleation of Methane Hydrate at Moderate Supersaturation Using Transition Interface Sampling

A. Arjun and P. G. Bolhuis\*

Cite This: *J. Phys. Chem. B* 2020, 124, 8099–8109

Read Online

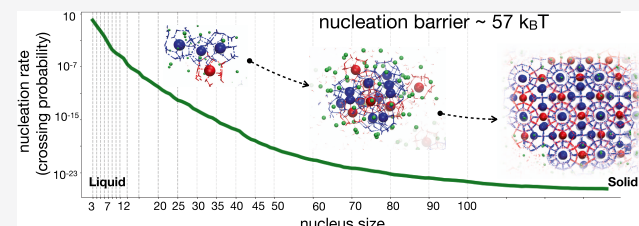
ACCESS |

Metrics & More

Article Recommendations

Supporting Information

**ABSTRACT:** The crystallization of methane hydrates via homogeneous nucleation under natural, moderate conditions is of both industrial and scientific relevance, yet still poorly understood. Predicting the nucleation rates at such conditions is notoriously difficult due to high nucleation barriers, and requires, besides an accurate molecular model, enhanced sampling. Here, we apply the transition interface sampling technique, which efficiently computes the exact rate of nucleation by generating ensembles of unbiased dynamical trajectories crossing predefined interfaces located between the stable states. Using an accurate atomistic force field and focusing on specific conditions of 280 K and 500 bar, we compute for nucleation directly into the sI crystal phase at a rate of  $\sim 10^{-17}$  nuclei per nanosecond per simulation volume or  $\sim 10^2$  nuclei per second per  $\text{cm}^3$ , in agreement with consensus estimates for nearby conditions. As this is most likely fortuitous, we discuss the causes of the large differences between our results and previous simulation studies. Our work shows that it is now possible to compute rates for methane hydrates at moderate supersaturation, without relying on any assumptions other than the force field.



## INTRODUCTION

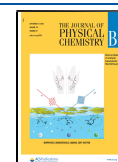
Mixtures of methane gas and water can spontaneously form a solid hydrate at low temperatures and/or high pressures due to hydrophobic interactions<sup>1</sup> in which the gas molecule stabilizes the encapsulating water cage.<sup>2</sup> Methane hydrates naturally occur in abundance at the ocean floors and in permafrost, exceeding the natural gas reserve substantially.<sup>3</sup> As such, methane hydrates are envisioned not only as a future energy resource<sup>4,5</sup> but also as very relevant for the stability of ocean floors<sup>6</sup> and global climate change.<sup>7</sup> In addition, interest in methane hydrates follows from the possible design of inhibitors that prevent hydrate formation in industrial pipelines.<sup>8</sup> A better understanding of the molecular mechanism of methane hydrate formation will be of interest to a large scientific audience.

Under moderate conditions, hydrates form via a nucleation and growth mechanism.<sup>9</sup> Such a hydrate formation mechanism can be understood within the framework of the widely used classical nucleation theory (CNT).<sup>10</sup> This theory postulates a spherical solid nucleus growing in a metastable liquid phase. The creation of a solid–liquid interface is unfavorable due to surface energy until the growing nucleus reaches a certain critical size to overcome the activation free energy barrier. From then on, the driving force toward the solid is large enough to allow spontaneous growth into a bulk crystalline phase. The thermodynamically stable crystal phase for methane hydrate is called structure type I (sI) and is composed of two standard methane cages in a ratio of 3:1. These cages are characterized by how their hydration shell is geometrically organized. The majority cage type  $5^{12}6^2$  is built from 12

pentagons and 2 hexagons, while the minority cage type  $5^{12}$  consists of 12 pentagons only. While the sI form is the most abundant in nature, methane hydrates can also form via a nonclassical mechanism in which an amorphous metastable intermediate (composed of nonstandard cages and with many fewer  $5^{12}6^2$  cages) precedes the formation of a crystalline state. Under natural conditions, hydrate formation will be mostly dominated by heterogeneous nucleation. Still, as a first step, it is essential to understand the homogeneous process.<sup>11</sup>

CNT successfully models homogeneous nucleation for many systems, not only giving a general expression for the barrier height, but also for the nucleation rate, defined as the number of nucleation events per unit volume and time. This value scales exponentially with the free energy barrier. Notwithstanding the success of CNT, a detailed understanding of the molecular mechanism of methane hydrate nucleation is still lacking, as current experimental analysis techniques are limited in spatiotemporal resolution and, hence, cannot directly give atomistic insight (although we note that recently breakthrough experiments were able to glean several nucleation features in other systems such as nanoparticles<sup>12,13</sup>).

Received: May 21, 2020  
Revised: August 11, 2020  
Published: August 17, 2020



Such insight into the molecular motions is fundamental in understanding and eventually controlling the kinetics and thermodynamics of the nucleation and growth process. Direct molecular dynamics (MD) simulations using atomistic force fields could in principle provide this knowledge and predict thermodynamic and kinetic properties. However, the current computer hardware can only access  $\mu\text{s}$ – $\text{ms}$  timescales even for a relatively small simulation volume. At moderate undercooling, where an experiment would still be able to observe homogeneous nucleation, the free energy barrier for nucleation is already large, leading to very long induction times in the small simulation volume and, thus, rendering straightforward MD utterly unfeasible. For instance, overcoming a barrier of roughly  $50 k_{\text{B}}T$  would already take billions of years of (wall clock) computer time. For a higher degree of undercooling or supersaturation, the driving force toward nucleation becomes stronger. That is why many simulation studies are performed at lower temperatures or higher supersaturation so that spontaneously nucleation is observed within a realistic simulation time.<sup>2,14–22</sup> At this high driving force, the nucleation process might be significantly different from the nucleation at higher temperatures, as recent experiments indicated.<sup>23</sup> As an illustration, simulations often find methane hydrates nucleating into amorphous phases, instead of the more thermodynamically stable sI phase. The formation of an amorphous phase is rationalized by Oswald's step rule,<sup>24</sup> which postulates the formation of an intermediate metastable phase with a different geometry before the thermodynamically stable state is reached.

Fortunately, nucleation of methane hydrates at moderate supersaturation can also be studied using enhanced sampling techniques and/or coarse-grained water models. For instance, Bi et al.<sup>25</sup> conducted forward flux sampling (FFS) simulations at a strong undercooling ( $T = 220 \text{ K}$ ), where they found the sII clathrate structure as the most dominant phase. Lauricella et al.<sup>26</sup> also reported sII clathrates based on a metadynamics study at moderate undercooling ( $T = 273 \text{ K}$ ). Later, DeFever and Sarupria<sup>18</sup> employed FFS to find (using a water-soluble guest at  $T = 230 \text{ K}$ ) the formation of an amorphous solid. In all of the above studies, the formation of the thermodynamically stable phase sI was never observed. Also, note that all of these studies used a coarse-grained model of water.<sup>27</sup>

Nucleation rate predictions for methane hydrates vary widely between  $2 \times 10^{21} \text{ nuclei cm}^{-3} \text{ s}^{-1}$  ( $T = 220 \text{ K}$ ,  $P = 500 \text{ bar}$ , using FFS)<sup>17</sup> and  $3 \times 10^{-111} \text{ nuclei cm}^{-3} \text{ s}^{-1}$  ( $T = 273 \text{ K}$ ,  $P = 900 \text{ atm}$ , using CNT with computed thermodynamic properties<sup>28</sup>), more than 132 orders of magnitude difference. Experimentally established nucleation rates range between  $3 \times 10^0$  and  $3 \times 10^{-7} \text{ nucleus cm}^{-3} \text{ s}^{-1}$  for various conditions.<sup>29–37</sup> Clearly, predicting accurate nucleation rates is notoriously difficult. Amongst others, the origins of the discrepancies could be due to the force field (atomistic or coarse grained), the choice of the collective variable (e.g., nucleus size metric<sup>38</sup>) in the enhanced sampling methods, system size, specific assumptions (e.g., which phase is formed), and of course thermodynamic conditions. Therefore, one would prefer to use an enhanced sampling method making the least amount of assumptions. Transition path sampling<sup>39</sup> is among those methods.

In this work, we apply transition interface sampling (TIS)<sup>40</sup> to compute the nucleation rate for realistic undercooling<sup>41</sup> ( $T = 280 \text{ K}$ ) at a relevant pressure ( $P = 500 \text{ bar}$ ), employing an accurate atomistic force field (Tip4P/ICE).<sup>42</sup> Recently, we

performed extensive transition path sampling (TPS)<sup>43</sup> simulations on hydrate nucleation in a methane/water mixture with an sI stoichiometry at moderate temperatures between 270 and 285 K at a pressure of 500 bar using the same system setup as in refs 2, 19, 21, 22. The melting point for the model used is  $303 \pm 2 \text{ K}$ .<sup>44</sup> In the metastable liquid state, the system is phase separated into a (super)saturated water–methane mixture in equilibrium with a (spherical) methane gas reservoir. The supersaturation is moderate, resulting in a large nucleation barrier. TPS circumvents the long induction times involved in the nucleation process while retaining the advantage of the unbiased dynamics by sampling an ensemble of MD trajectories connecting the liquid and (amorphous or crystalline) solid states. Analysis of this path ensemble showed that the nucleation pathways switch from forming only amorphous solid hydrates to a crystallization mechanism ending in the sI state. Interestingly, at 280 K, both mechanisms can coexist. Now, while TPS does not directly give access to the nucleation rate nor the free energy barrier, the efficient TIS extension of TPS is capable of doing so.<sup>40</sup> TIS computes the flux through a series of interfaces between the liquid and solid states, yielding the total rate constant. The TIS algorithm has been applied before to crystallization in Lennard-Jones models<sup>45</sup> and colloidal systems<sup>46</sup> and was recently employed to study the solidification of Ni.<sup>47</sup> In general, path sampling techniques are more robust to estimate rates, avoiding any approximations made by CNT. For instance, the rate of nucleation of ice from water (a process related to hydrate formation) was rigorously measured by sampling the pathways along the nucleation barrier.<sup>48</sup>

Here, we compute the nucleation rate of methane hydrate to be  $\sim 10^2$  nuclei per second per  $\text{cm}^3$ , for a moderate undercooling of 280 K and a pressure of 500 bar, in rough agreement with the known experimental values. Knott et al. estimated almost 120 orders of magnitude lower rate under nearby conditions,<sup>28</sup> which essentially ruled out the presence of homogeneous nucleation due to the very high free energy barrier obtained. We argue that this discrepancy can be explained to a large extent by the difference in the system setup used in the simulations. Our findings suggest that homogeneous nucleation, while unlikely to be realistic under natural conditions, could still be relevant for moderate undercooling and high pressure. Most importantly, this study shows that it is now possible to obtain accurate crystal nucleation rates at moderate supersaturation and, thus, for a high free energy barrier, without influence due to the choice of the progress variable, and without any assumption, except for the force field.

The remainder of this article is organized as follows. In **Methods** section, we introduce the methods and system setup. In **Results and Discussion** section, we discuss the results, followed by conclusions in the section **Conclusions**.

## METHODS

**Transition Interface Sampling.** TIS belongs to the TPS family of Monte Carlo-based algorithms for creating ensembles in trajectory space.<sup>49</sup> The TIS algorithm was specifically developed to compute the kinetic rate constants for rare events more efficiently than the original TPS algorithm, which required a slow transformation of an unrestricted path ensemble into the rare event path ensemble.<sup>50</sup> To do so, TIS introduces a set of  $n$  nonintersecting interfaces, placed along a reasonable order parameter or collective variable capable of separating the stable states. In the TIS framework, the rate

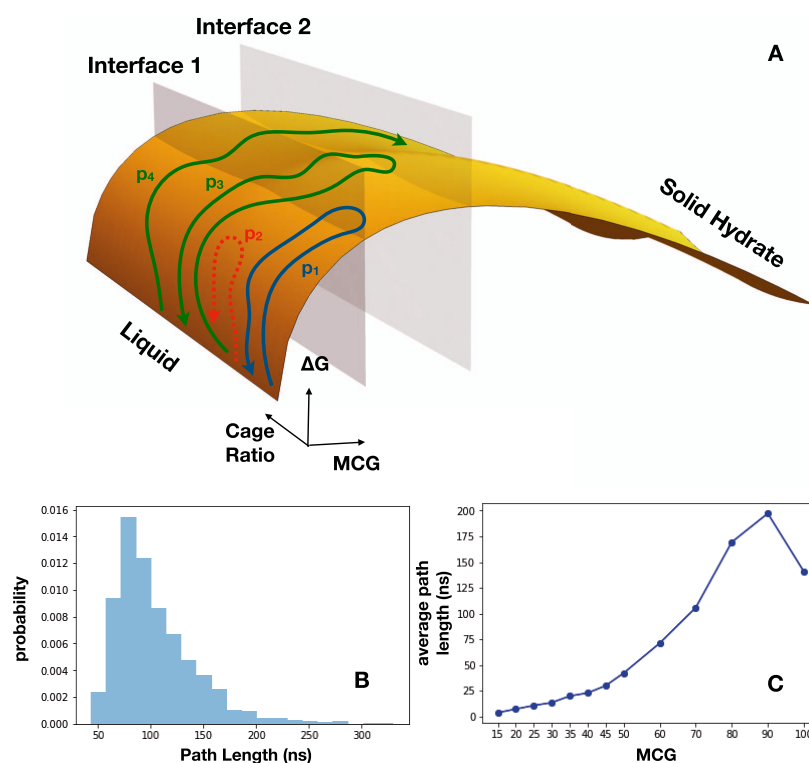


**Figure 1.** (A) Schematic of the nucleation free energy barrier as a function of nucleus size (MCG) and cage ratio, combined with the general scheme for TIS simulations. The barrier crossing can be sampled by defining interfaces, indicated by the transparent surfaces. For each interface, TIS sample pathways under the conditions that they start in the liquid state and end in either the solid or the liquid state. Path p1 (blue curve) represents a successful TIS path that belongs to interface 1. Trial path p2 (red curve) is rejected as it does not cross interface 1. Green paths p3 and p4 belong to interface 2. Path p3 is a liquid-to-liquid trajectory that passed interfaces 1 and 2 and eventually returns to the liquid state. Path p4 crosses interface 2 and ends up in the solid state. (B) Path length distribution for an interface at MCG = 70. Path length distribution for other interfaces is given in the Supporting Information (SI). (C) Average path length at first increases with MCG, but decreases again beyond the critical nucleus, as paths become committed to the final state.

constant is viewed as the flux of trajectories through the final interface  $n$  (equivalent to state B), which in turn can be written as the product of the flux through the first interface, and the so-called crossing probability

$$k_{AB} = \Phi_{n,0} = \Phi_{1,0} P_A(n|1) = \Phi_{1,0} \prod_{i=1}^{n-1} P_A(i+1|i) \quad (1)$$

Here, interface 0 defines state A and interface  $n$  delineates the boundary of state B. In the final equation, the rate is thus composed of two ingredients. The first factor  $\Phi_{1,0}$  is the flux of trajectories through the first interface, the one closest to A. The second factor  $P_A(i+1|i)$  is the probability that trajectories coming from state A and crossing interface  $i$  are able to reach interface  $i+1$ . For each interface  $i$ , path sampling is used to estimate this crossing probability  $P_A(i+1|i)$  under the conditions that all trajectories cross the interface  $i$  and come directly from the initial state A. To generate new pathways, a shooting algorithm similar to standard TPS creates forward and backward trial MD trajectories from a randomly selected frame, which can be accepted based on a Metropolis criterion.<sup>49,51</sup> For efficiency, TIS allows flexible lengths of pathways, which can be halted as soon as the paths reach a stable state or cross the required interface. We apply the Gaussian biased shooting scheme, which selects shooting points close to the interface leading to higher acceptance of paths.<sup>51</sup> In TIS, the location of the interfaces is an important aspect of sampling. Interfaces should neither be too close nor

too far from each other. Hence, the location of the interfaces needs to be optimized, usually by trial and error. This makes it hard to parallelize the methods. Therefore, we use a slightly different TIS implementation, where all trajectories are continued until they reach stable state A or B. Thus, all paths are either leading from A to A or from A to B. Note that this is the standard implementation in the OpenPathSampling (OPS) software package.<sup>52,53</sup> The general scheme of the TIS implementation is illustrated in Figure 1.

To enhance the decorrelation of pathways, the replica exchange TIS algorithm (RETIS) allows for the exchange of paths between neighboring interfaces.<sup>51,54–56</sup> In combination with a move that samples the initial state, RETIS enhances the path sampling of the path space tremendously.

#### System Setup, Force Field, and Simulation Details.

Our system consists of a cubic box with 2944 water and 512 methane molecules. Water was represented by the TIP4P/Ice model,<sup>57</sup> and methane was modeled using united atom Lennard-Jones interactions ( $\epsilon = 1.22927$  kJ mol<sup>-1</sup> and  $\sigma = 3.700$  Å). This combination has been shown previously to mimic experimentally determined properties very well.<sup>44</sup>

Most of the molecular dynamics (MD) simulations were performed using OpenMM 7.1.1.<sup>58</sup> The Velocity Verlet with the velocity randomization (VVVR) integrator (from openmmtools<sup>59</sup>) was used to integrate the equations of motion. The integration time step was set to 2 fs. The van der Waals cutoff distance was 1 nm. Long-range interactions were handled by the Particle Mesh Ewald technique. The MD



simulations were performed in the NPT ensemble using the VVVR thermostat (frequency of 1/ps) and a Monte Carlo barostat (frequency of 4 ps). TIS simulations were performed using the CUDA platform of OpenMM on NVIDIA GeForce GTX TITAN 1080Ti GPUs. TIS was executed using the OpenPathSampling<sup>52,53</sup> package.

**Order Parameters and Collective Variables.** *Nucleus Size Parameter.* We employ the size of the largest solid cluster as the order parameter to place the interfaces. The size of the nucleus has been used previously in simulation studies<sup>17,47,48</sup> to calculate the rate of nucleation. The mutually coordinated guest (MCG) order parameter<sup>60</sup> counts the number of methane molecules involved in the largest solid nucleus in the nucleating hydrate system. Each methane molecule (guest molecule) is checked whether its neighboring (methane and water) molecules satisfy a set of geometric constraints.<sup>60</sup> If so, then methane is an MCG monomer. Neighboring MCG monomers are part of the same cluster. The largest connected cluster in the system is then identified using a cluster algorithm. The MCG order parameter is defined as the size of this largest (solid) cluster. Here, we use MCG-1 (and refer it to as MCG) as it checks for any possible occurrence of nucleus formation compared to MCG-3, which only identifies the stable nucleus.<sup>60</sup> We determined the MCG using a home-written analysis code.

*Cage Type Analysis.* The structure of the growing nucleus can be identified by cage types that form it. We analyze the cage type for each methane in the MCG-based cluster using an algorithm similar to the one employed in ref 61, using a home-written code. We identified seven main types of cage structures, namely,  $5^{12}$ ,  $5^{12}6^2$ ,  $5^{12}6^3$ ,  $5^{12}6^4$ ,  $4^15^{10}6^2$ ,  $4^15^{10}6^3$ , and  $4^15^{10}6^4$ , where the superscript indicates the number of polygons made by the hydrogen-bonded water molecules in the cage facet. The base number gives the type of polygon (4: square, 5: pentagon, 6: hexagon). The ratio of the number of  $5^{12}6^2$  and  $5^{12}$  cages denotes the cage ratio (CR) parameter, which can be used as an indicator of sI crystallinity and has been employed previously.<sup>16,26,62,63</sup> This cage ratio is CR = 3 for a perfect sI methane hydrate, and lower than unity, CR < 1, for an amorphous or sII structure. Note that previous studies have mostly focused on transition paths that end with CR < 1, characteristic of the amorphous or sII phase.<sup>15,17,26</sup> This effectively means that we identify noncrystalline clusters as amorphous (including sII).

**Stable State Definition.** The acceptance criterion for TIS requires a definition of the stable states. Here, we define the liquid stable state by the absence of any cluster larger than a dimer,  $MCG \leq 2$ . We define the solid stable state by the presence of the largest cluster size  $MCG \geq 200$  methane molecules. An important aspect is that these stable state definitions do not fix the final solid state to be amorphous, crystalline sI, or even sII. All structures are acceptable as the final state in the path sampling and the system is free to choose, which is more favorable.

There is a small chance that the spherical methane reservoir takes on a cylindrical shape, due to the relatively small simulation volume (especially during the RETIS minus move). When this occurs, the thermodynamic conditions drastically change, and we are effectively in another regime. Since we are not interested in sampling phase transformation in the regime of the cylindrical reservoir, we avoid this regime by checking for a cylindrical reservoir shape and reject trial paths for which

this transition occurs. More information is provided in the [Supporting Information](#).

**TIS and RETIS Simulation Details.** The MCG order parameter acts as a progress variable to define the interfaces along the nucleation process. Even though the use of path sampling speeds up the sampling exponentially, the average duration (length) for a full transition path from liquid-to-solid at 280 K and 500 bar pressure is in the order of a few hundred nanoseconds. This makes the path sampling computationally expensive, requiring the use of GPUs. Due to I/O and storage space limitation, we use a saving frequency of 100 ps, i.e., during the MD simulation, the snapshots of the system are stored only once every 100 ps. This relatively low saving frequency should not affect the mechanism or the rate constant, as the average transition time is already hundreds of nanoseconds, and the residence time is many orders of magnitude longer. Indeed, the resulting rate from TIS is independent of saving frequency, as a lower flux, due to missed interface crossings for lower frequencies, is compensated by an increase in the crossing probability for the final interface. Note that the low saving frequency might lead to large jumps in the order parameter from one frame to the next. The effect of such jumpiness has been studied in the context of FFS in ref 64.

The interfaces for regular TIS were set at 13 different locations along the MCG order parameter, as given in [Table 1](#). The choice for these values was based on the requirement for a sufficient overlap of the crossing histograms from one interface to the next. That is, paths that are sampled in interface  $i$  should have a reasonable chance of reaching interface  $i + 1$ . The rule of thumb for TIS is that this probability should be roughly

**Table 1. Sampling Details for 24 Interfaces<sup>a</sup>**

MCG	<path length> (ns)	acceptance	decorrelation
3	0.35	2097/3174 (66.0)	28
4	0.39	2162/3047 (70.9)	94
5	0.42	2009/3105 (64.7)	62
6	0.43	2029/3071 (66.0)	26
7	0.46	1937/3032 (63.8)	17
8	0.76	1698/3029 (56.0)	40
9	0.85	1756/3207 (54.7)	105
10	0.87	1682/3111 (54.0)	100
11	0.86	1711/3120 (54.8)	101
12	1.41	1539/3091 (49.7)	95
13	2.15	1577/3134 (50.3)	128
15	3.62	2767/5000 (55.3)	221
20	7.12	2684/5000 (53.6)	218
25	10.62	2676/5000 (53.5)	258
30	13.4	2838/5000 (56.7)	265
35	19.79	1350/2399 (56.2)	161
40	22.8	1659/3060 (54.2)	102
45	29.9	2150/3625 (59.3)	176
50	42.2	2897/5000 (57.9)	407
60	71.2	1094/1830 (59.7)	195
70	105.8	721/1119 (64.3)	145
80	169.4	518/838 (61.8)	116
90	197.30	182/354 (51.4)	48
100	140.9	541/968 (55.8)	113

<sup>a</sup>The first 11 interfaces are sampled using RETIS. The third column gives the number of accepted paths, the number of trials, and the acceptance ratio (in percentage) in brackets. The last column gives the number of decorrelated paths.

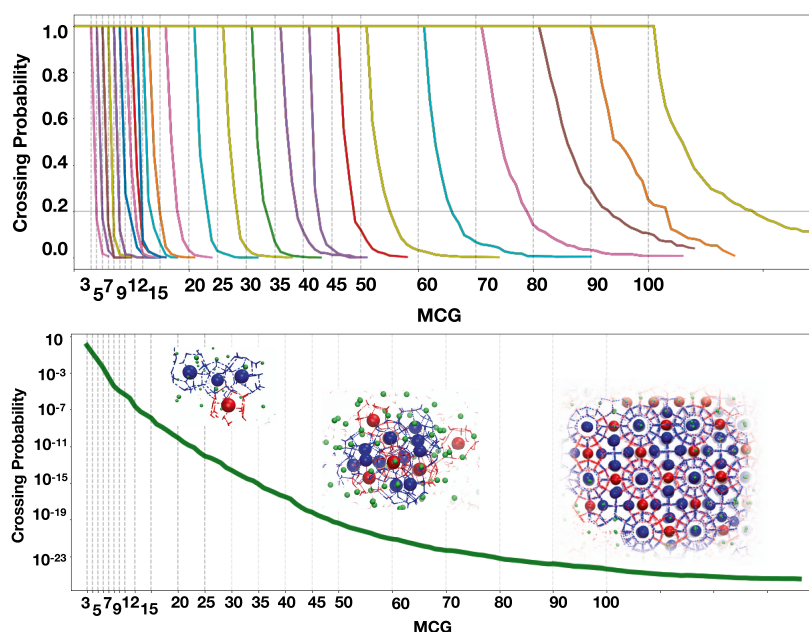


**Figure 2.** Top: the individual crossing probabilities for each sampled interface plotted along the progress order parameter MCG. Vertical lines indicate interface locations. The horizontal line (in gray) demarcates the 0.20 threshold for the next interface. Bottom: the total crossing probability (TCP) along the progress parameter MCG, joined using WHAM. The TCP curve plateaus at  $2.7 \times 10^{-26}$ . The snapshot insets depict the growth of the nucleus. Blue and red cage represent  $S^{12}6^2$  and  $S^{12}6^2$ , respectively. Methane gas trapped inside is also shown in the same colors. The green spheres around the fully formed cages show the MCG molecules part of the growing cluster but yet to form cages.

0.20. However, due to the steepness of the barrier (especially in the beginning), this is not always the case.

As an initial path to kickstart the TIS sampling, we take a full TPS path that nucleated into an sI crystal.<sup>43</sup> We applied the one-way shooting move, where the shooting points were selected from a Gaussian distribution in the MCG variable, centered around the interface value, with a width parameter of  $\alpha = 0.03$ . More information is provided in the [Supporting Information](#). [Table 1](#) gives the TIS sampling details in terms of the number of trial shots, the acceptance ratios, the average path length, and the number of decorrelated paths. The total aggregate simulation time was 1.2 ms, which took a total of 15 months of wall clock time on our GPU setup.

At interfaces with low MCG values, paths tend to become very short, often below a ns, resulting in a reduced path decorrelation. Replica exchange TIS (RETIS) can significantly enhance this decorrelation. Therefore, we performed an independent RETIS simulation run for the interfaces MCG = 3–13. In total, 50 000 MC moves were performed with an average acceptance of 60%. The path exchange move was attempted 2266 times and the minus move 1188 times (with 100% acceptance<sup>54</sup>).

## RESULTS AND DISCUSSION

**Sampling Interfaces and Extracting the Crossing Probability.** We performed transition interface sampling (TIS) of methane hydrate nucleation at a realistic temperature of 280 K and a relevant pressure of 500 bar, using the same system setup as in ref 43. The acceptance ratio and the number of decorrelated paths are given in [Table 1](#). Selected path trees are shown in the [SI](#).

The crossing probabilities as a function of MCG were recorded for each of the TIS and RETIS ensembles and are depicted in [Figure 2](#). Clearly, the crossing probabilities steeply decrease with MCG, certainly at the lower interfaces, but level

off for higher interface values, where the barrier becomes flatter, as is expected when the critical nucleus is reached. The steepness at the interfaces with lower MCG values is also the reason that the interfaces are placed closer together there. Although not every TIS run showed the optimal 20% crossing with the next interface, there is a significant overlap between each successive interfaces so that we can apply the Weighted Histogram Analysis Method (WHAM)<sup>65</sup> to join the histograms. [Figure 2](#) shows the resulting total crossing probability. Here, the log probability indeed exhibits an initial steep decrease that slowly becomes flatter for higher interfaces. We estimated the error bar in the final crossing probability using the bootstrapping method to be 1–2 orders of magnitude (see the [SI](#)).

**Flux Calculation.** The flux out of the liquid state (defined by  $MCG \leq 2$ ) through the first interface at  $MCG = 3$  is computed from the RETIS simulation by summing the average path lengths of the minus and the first interface,<sup>66</sup> as implemented in OPS.<sup>52,53</sup> This average path length is around five frames, which, with a saving frequency of 100 ps, translates into 500 ps on average. The flux through  $MCG = 3$  is thus  $\Phi_{3,2} = 0.002 \pm 0.00008 \text{ ps}^{-1}$ . Note that this flux will be dependent on the saving frequency and should be matched with a crossing probability obtained with the same saving frequency.

**Nucleation Rate Calculation.** The product of the flux and the crossing probability leads directly to the nucleation rate. As nearly all paths for the interface  $MCG = 110$  end in the solid state (shown in the [Supporting Information](#)), the crossing probability will not change anymore beyond that interface. Therefore,  $k_{AB} = \Phi_{3,2} P_A(13813) = 0.002 \times 2.7 \times 10^{-26}$  nuclei per picosecond per simulation volume. The error on this number is mostly caused by the uncertainty in the crossing probability. Indeed, the bootstrapping results indicate that the error in the rate constant is roughly 1–2 orders of magnitude (calculation shown in the [SI](#)).

As this rate is the expected homogeneous nucleation events per unit time in the simulation volume, we can easily estimate the rate in terms of the number of nuclei per second per cubic cm. Assuming that each nucleation events are independent of each other, this is simply determined by the size of the used simulation box. For our simulation, the box volume  $V = 110.5 \text{ nm}^3$ , yielding an overall nucleation rate of  $J_{\text{TIS}} = k_{\text{AB}}/V = 5.08 \times 10^2 \text{ nuclei cm}^{-3} \text{ s}^{-1}$  (Table 2). The computed nucleation

**Table 2. Nucleation Data from TIS Simulations**

flux through MCG = 3 (nuclei ps <sup>-1</sup> )	0.002
crossing probability	$2.77 \times 10^{-26}$
average liquid phase volume, $V_{\text{liq}}$ (nm <sup>3</sup> )	110
nuc. rate from TIS, $J$ (nuclei cm <sup>-3</sup> s <sup>-1</sup> )	$5.08 \times 10^2$
monomer number density, $\rho$ (cm <sup>-3</sup> )	$5 \times 10^{20}$
Zeldovich factor, $Z$	0.025
diffusivity, $D$ (MCG <sup>2</sup> /ns)	7.8
nucleation barrier, $G(n)/k_{\text{B}}T$	56.9
nuc. rate from CNT, $J_{\text{CNT}}$ (nuclei cm <sup>-3</sup> s <sup>-1</sup> )	$2 \times 10^4$

rate will be similar for both the amorphous and the crystalline channel of the hydrate nucleation at the imposed temperature, as, in our previous TPS study, we found an equal population of amorphous and crystalline pathways.

**Free Energy and Comparison with CNT.** As many simulation studies focus on the free energy barrier and employ CNT to estimate the rate, it is natural to compare our TIS rate prediction to an estimate based on the free energy barrier. The TIS simulation of the nucleation process does not give the free energy barrier directly because the pathways that come from a high MCG value (the B state) are missing from the sampling. To obtain an estimate of the free energy, we therefore performed several TIS simulations for the reverse process, i.e., starting at a post-critical value of  $\text{MCG} > 100$  and traversing the barrier in the reverse direction (see the SI for details). The crossing probabilities for the reverse process can be found in the SI. Note that the reverse paths only start sampling BA paths around  $\text{MCG} = 95$ . By reweighing all paths according to their true path probability, we obtain the reweighted path ensemble,<sup>67,68</sup> which we can subsequently project on the MCG variable. Doing this for the forward and reverse path ensembles leads to the estimated free energy curve in Figure 3. The zero of the curve is obtained from histogramming a straightforward MD simulation (see the SI for more information). The maximum of the free energy curve is located at  $\text{MCG} = 90$ , where the barrier height is roughly 56.9 kT, in agreement with our previous TPS result that located the critical nucleus between  $\text{MCG} = 80$  and 100.<sup>43</sup> The error in the free energy is mostly determined by the error in the crossing probability, which is analyzed in the SI. The error in the free energy is estimated to be roughly 1.25  $k_{\text{B}}T$ . From a mean square distance analysis on the top of the barrier, we measured a diffusion constant of  $D \approx 7.8 \text{ MCG}^2/\text{ns}$  (see the SI for more information). The Zeldovich factor is the probability to reach the final state from the barrier and can be computed from the crossing probability. We find for the barrier location  $Z \approx \exp(-3.7) \approx 0.025$ . Finally, the average number of methane molecules in the liquid phase gives the monomer density  $\rho = 60/V_{\text{liq}} = 5 \times 10^{20} \text{ cm}^{-3}$ .

The rate predicted from this analysis is thus  $J = 7.8\rho Z e^{-56.9} = 2 \times 10^4 \text{ nuclei cm}^{-3} \text{ s}^{-1}$ . This is less than two orders of magnitude higher than the rate based on TIS. Considering the

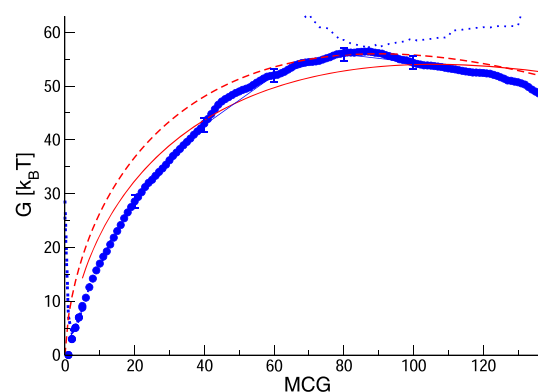


**Figure 3.** Free energy from projecting the reweighted path ensemble (blue circles). Error bars are estimated from the error in the crossing probability. Dashed blue curves are the partial densities from the forward and reverse path ensembles. Red curves are plots from standard CNT expressions: the solid curve is the best fit to the simulation data; the dotted red curve is a fit to the maximum of the barrier.

error bars in the simulations, we deem this as a very good agreement. We believe that the TIS result is more trustworthy as it does not rely on any approximation.

In the same plot, we also give the free energy using the standard CNT expression (red dotted curve), such that the location of the maximum coincides with our simulation results. This requires a driving force and surface tension that are a factor 1.6 smaller than we previously estimated.<sup>43</sup> Moreover, this estimated curve deviates strongly from the free energy obtained for TIS, well outside the estimated error bar. The best fit to the data (solid red curve) is also substantially different. We conclude that the CNT expression is only an approximate, qualitative description for the hydrate nucleation free energy at these conditions.

**Molecular Mechanism of Nucleation.** All pathways in the TIS ensembles start in the metastable liquid phase and progress up the nucleation barrier until they cross the imposed interface and relax back to the liquid phase or continue until full solidification. Previously, we found that the nucleation mechanism shifts from forming amorphous phases at lower temperatures to sI crystal formation at higher temperatures. At 280 K, both mechanisms can coexist.<sup>43</sup> The two mechanisms can be identified by the cage ratio CR, the ratio of large and small cages, which is higher than unity for crystalline structures and lower than 1 for amorphous structures. While the cage ratio is not the only indicator of crystallinity, e.g., the connectivity of the  $5^{12}6^2$  cages is also indicative of an sI crystal. However, we observe in all trajectories that the large  $5^{12}6^2$  cages always form into a connected, spherical grid, that is part of a single growing cluster (see also movies provided in the SI).

We analyzed close to 2.5 million frames from the TIS simulated pathways and plotted histograms of the cage ratio for several path ensembles in Figure 4. At the lower interfaces, paths are only sampling amorphous structures, but when reaching interfaces closer to the critical nucleus, the histograms clearly show signatures of crystallinity. Note that this observed behavior might change for a different progress variable. We, however, stress that the final result of TIS is independent of the choice of the order parameter.

**Comparison to Previous Rate Predictions.** Naturally, our rate predictions should be compared to the experimental



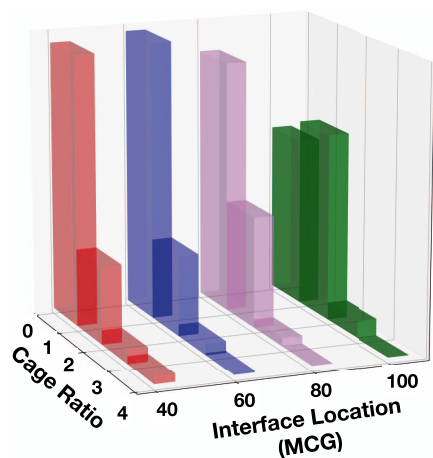


**Figure 4.** Cage ratio histogram for selected interfaces. A total of 2.5 million frames were analyzed, which included the data from all of the interfaces (shown in the SI). The amorphous phase is identified by a cage ratio < 1 (corresponding to the first bar at any interface value). There is a gradual shift in the population of the cage ratio from lower (MCG = 40) to higher (MCG = 100) interfaces. At MCG = 100, crystalline nuclei become the most abundant. (Also, see Figure S11 in the Supporting Information).

results as well as previous predictions. The experimentally found nucleation rates vary widely, and trustworthy measurements at the conditions used here do not exist. However, experiments at ambient conditions give nucleation rates of  $10^0$ – $10^{-7}$  nuclei  $\text{cm}^{-3} \text{s}^{-1}$ .<sup>30–37,30–37</sup> Our predicted rate is 5–9 orders of magnitude higher, which is consistent with the higher pressure imposed in our work.

The nucleation rate is highly sensitive to both the pressure and the methane supersaturation or, equivalently, the chemical potential of the dissolved gas. The chemical potential or fugacity, the driving force for nucleation, in turn is determined by the external pressure and temperature.

While it is practically impossible to measure homogeneous nucleation rates in methane hydrates under high pressure, Thoutam et al.<sup>29</sup> evaluated several models for homogeneous nucleation based on CNT using six different fugacity setups, consistent with the experimental results. They found a rate of nucleation between  $1.35$  and  $7.60 \times 10^0$  nuclei  $\text{cm}^{-3} \text{s}^{-1}$  for 280 K and pressure close to our simulation (30 MPa). These values are within the statistical error of our rate predictions.

Other simulation-based nucleation rate predictions reported in the literature are 21–33 orders of magnitude higher than the experimental ones.<sup>17,18,20</sup> This can be explained by a reduced nucleation barrier as these simulations were performed at much lower temperatures of 220–250 K. Indeed, our TPS simulations also showed that the nucleation barrier reduces with the decreasing temperature.<sup>43</sup>

On the other hand, Knott et al.<sup>28</sup> predicted for 273 K and 900 atm, an exceedingly small rate that is 100 orders of magnitude lower than our prediction and the values reported in ref 29. While the conditions differ slightly from the pressure and temperature used here, this difference is not sufficiently large to explain the enormous discrepancy with our prediction.

Instead of the nucleation rate, we can also compare the corresponding free energy barriers. The predicted free energy barrier based on the TIS simulations was  $\approx 56.9 \text{ k}_B\text{T}$ . The two previous estimates for the nucleation free energy barrier close to these conditions are 173<sup>26</sup> and 300  $\text{k}_B\text{T}$ .<sup>28</sup> Several

arguments can be put forward to explain these large discrepancies in the rate and free energy barrier. First, we notice that the simulation setup was different. Due to the necessity for a limited system size, the choice of stoichiometric conditions, and the need for a complete solidification in our path sampling simulations, the methane reservoir in the initial state is a bubble with a radius on the order of a few nanometers. This leads to an additional Laplace pressure that induces a higher methane solubility and, hence, a higher driving force. This higher driving force naturally leads to a lower barrier and a higher rate and contributes to the difference with the work of Knott et al.<sup>28</sup> and of Lauricella et al.<sup>26</sup>

As in our previous work,<sup>43</sup> we can estimate the driving force as  $\Delta\mu = 2\gamma/(\rho_s r^*)$ , from the observed radius of the crucial nucleus  $r^*$ , the surface tension of the liquid–crystal interface  $\gamma$ , and the density of the solid nucleus  $\rho_s$ . Setting  $\gamma \approx 32 \text{ mJ m}^{-2}$ ,<sup>69,70</sup> and  $\rho_s = 4.57$  (in units of cages per  $\text{nm}^3$ ),<sup>43</sup> and using the relation between size and number of methane molecules  $(4/3)\pi\rho_s r^{*3} = n^*$ , the observed critical nucleus  $n = 90$  yields a system driving force  $\Delta\mu^{\text{sys}} \approx 5 \text{ kJ mol}^{-1} \approx 2\text{k}_B\text{T}$ . The presence of the spherical bubble induces a Laplace pressure of roughly 750 bar,<sup>43</sup> which in turn gives an excess chemical potential  $\Delta\Delta\mu = \text{k}_B\text{T} \ln(P_{\text{bubble}}/P) \approx 0.92 \text{ k}_B\text{T}$ . The driving force in the absence of the bubble is thus  $\Delta\mu^{\text{flat}} = \Delta\mu^{\text{sys}} - \Delta\Delta\mu \approx 1.1 \text{ k}_B\text{T}$ , in line with the previous estimates.<sup>71</sup> Employing the CNT expression  $\Delta G^* = (16/3)\pi\gamma^3/(\rho_s\Delta\mu)^2$ , the barrier due to the Laplace pressure of the spherical bubble is a factor of 3–4 lower compared to a reservoir with a flat interface. With a predicted CNT barrier of 90  $\text{k}_B\text{T}$  for the spherical reservoir,<sup>43</sup> this would mean around 300  $\text{k}_B\text{T}$  for the flat gas–liquid interface. For our TIS computed barrier of  $\sim 60 \text{ k}_B\text{T}$ , this would still mean around 200  $\text{k}_B\text{T}$ . Adjusting the TIS-based barrier height for the flat interface thus brings the free energy much more in line with that of ref 28. We note that these barrier estimates are very rough and should not be taken as accurate quantitative predictions. However, in any case, with such high barriers, we expect homogenous nucleation not to play a significant role in the imposed moderate supersaturation conditions with a flat gas–liquid interface.

Besides the extreme difference in rates based on the used models, system setup, and conditions, there are also more subtle explanations for differences in results. For instance, there is a difference between the FFS and the TIS approach. Previously, FFS has been used for methane nucleation (using CG models). However, while TIS creates full trajectories that are able to relax in path space, the (direct) FFS approach could be (and often is) influenced by the choice of the interfaces. This can force the paths into the wrong direction in trajectory space, and lead to underestimation of the rate constant, and even to errors in the mechanistic interpretation.<sup>72,73</sup> This could explain why several FFS studies fail to find crystal nucleation toward the sI phase but rather predict the formation of an amorphous (or at least a noncrystalline) nucleus.<sup>17,18</sup> Of course, one could argue that the TIS simulation, starting with an initial trajectory that formed an sI crystal, could artificially get stuck in the crystalline channel, as the path sampling might not allow relaxation to the amorphous phase. However, we believe that this is not the case as our previous TPS simulations did exhibit switching between the amorphous and crystalline channels, and we expect that also the TIS will eventually sample the amorphous barrier. Since the barrier is roughly

Table 3. Comparison of the Predicted and Experimental Data<sup>a</sup>

<i>T</i> (K)	<i>P</i> (bar)	system (W/G)	method	FF	rate (cm <sup>-3</sup> s <sup>-1</sup> )	refs
220	500	6912/1280 (F)	FFS	mW	6 × 10 <sup>21</sup>	Bi <sup>17</sup>
230	500	7555/445 (F)	FFS	mW	1.3 × 10 <sup>26</sup>	DeFever <sup>18</sup>
250	500	2944/512 (B)	MD	T4I	5 × 10 <sup>25</sup>	Zhang <sup>19</sup>
250	300	2944/512 (B & F)	MD	T4I	5 × 10 <sup>24</sup>	Walsh <sup>20</sup>
255	500	2944/512 (B)	MD	T4I	9.43 × 10 <sup>23</sup>	Yuhara <sup>21</sup>
255	500	2944/512 (B)	MD	T4I	9.07 × 10 <sup>23</sup>	Barnes <sup>22</sup>
273	911	70 000 (F)	MD/CNT	mW	3 × 10 <sup>-111</sup>	Knott <sup>28</sup>
273	0.98	exp			10 <sup>0</sup> –10 <sup>-7</sup>	refs30–37
280	300	exp/model			3 × 10 <sup>0</sup>	Thoutam <sup>29</sup>
280	500	2944/512 (B)	TIS	T4I	5 × 10 <sup>2</sup>	this work

<sup>a</sup>System details for computational methods include the number of water (W) and guest (G) molecules used, the type of liquid–gas interface (flat (F) or bubble (B)), the water force field (FF) (T4I:Tip4P/Ice). Note that ref 20 uses the multiple system sizes where the rate varies between 10<sup>24</sup> and 10<sup>26</sup>. Ref 28 reports the total number of particles on the order of 70 000.

equal for both the crystal and amorphous phases at 280 K, we do not expect a difference in the rate.

Finally, we note that previous rate predictions for moderate undercooling are usually computed by indirect means. They are either based on CNT using several thermodynamic ingredients obtained from different sources or they employ a free energy calculation as a function of a fixed-order parameter. In contrast, our approach is an internally consistent approach that is not dependent on the choice of the order parameter. Instead, it just depends on the choice of the force field and the thermodynamic conditions imposed.

Table 3 summarizes several previous simulation-based predictions for homogeneous methane hydrate nucleation rates. The methodology and force fields used for each prediction was slightly different. Each study also used a different setting like undercooling (and pressure), but overall the nucleation rates are at least 20 orders away from the experimentally available results. Our results, performed at 280 K, are much more in line with the available experimental data.

Although this seems to suggest that at natural, moderate undercooling conditions, the homogenous nucleation of methane hydrate is feasible, the larger supersaturation due to the spherical gas bubble, together with the finite size scaling argument, leads to effectively much larger barriers for reservoirs with flat interfaces. The fact that experimental results are in line with our results must thus be interpreted as fortuitous. Indeed, ref 29 employed a slightly lower surface tension, which could have resulted in an overestimate of the experimental nucleation rate. Moreover, many experimental results refer to hydrates in general<sup>30–35</sup> and/or to heterogeneous nucleation<sup>36,37</sup> and, thus, cannot easily be compared.

To estimate how the predicted rate will change with temperature, we can use a simple approximation based on CNT, which states that the log rate is  $\ln J \sim -\Delta\mu^{-2} + \text{const}$ , where the proportionality factor and constant involve the kinetic prefactors, and properties such as the surface tension, which we assume constant over the temperature region of interest. We further assume that the driving force is given by  $\Delta\mu = \Delta S (T_m - T) + \Delta\Delta\mu$ , where  $\Delta S$  is the difference in the entropy of the liquid and the solid phases, and  $\Delta\Delta\mu$  is the additional driving force due to the curved interface (see the SI for further details). We can fit this relation to match both the TIS rate and the rate predictions from refs 17, 18, 20, which were done for the same system setup and pressures. Figure 5 plots the resulting fit of the temperature, together with the TIS

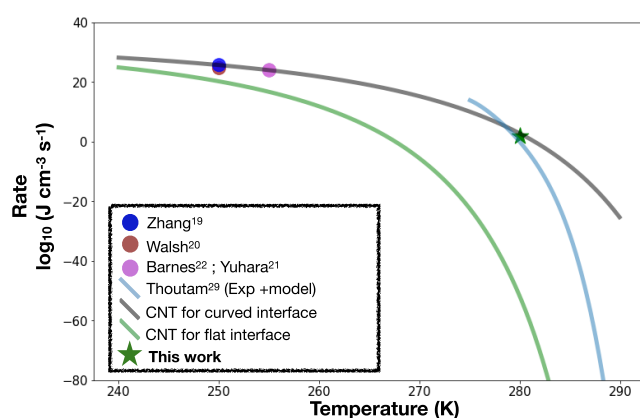


Figure 5. Temperature dependence of the logarithmic nucleation rates. Our rate prediction (green star) fortuitously matches the findings of ref 29 (light blue curve). The black curve is the CNT rate prediction for a curved interface, fitted to the simulated rates (circles and star). The green curve is the CNT corrected for a flat interface.

rate, and the rate predictions from refs 17, 18, 20 as well as the consensus estimate from ref 29. Naturally, the fitted (black) curve agrees well with the literature results. However, the slope for this curve is lower than the experimental data as due to the additional driving force of the curved interface the rate remains finite even at the melting temperature. Therefore, we also include the CNT-based green curve for a flat interface, which is estimated by subtracting the additional driving force due to the spherical bubble. The rate of nucleation for a flat interface is thus substantially smaller and behaves more similarly to the results from ref 29. However, due to the various assumptions in these CNT estimates and the strong sensitivity of the rate, it is not clear whether or not this is incompatible with the conclusion that nucleation is unfeasible.<sup>28</sup> In the SI, we present several other CNT-based curves, which all show similar behavior. We stress once more that all of these CNT predictions should be taken as qualitative.

## CONCLUSIONS

Understanding the nucleation kinetics of methane hydrates is of importance for both theoretical and practical reasons. We have presented extensive transition interface sampling simulations using an accurate atomistic force field. The TIS methodology enables an efficient evaluation of the exact rate of nucleation by generating ensembles of unbiased dynamical



trajectories, leading from the metastable liquid up to the nucleation barrier. For the imposed specific conditions of 280 K and 500 bar, we find a nucleation rate of  $\sim 5 \times 10^2$  nuclei per  $\text{cm}^3$  per second, which is, probably fortuitously, in agreement with a comparative analysis study.<sup>29</sup>

This study shows that it is now possible to obtain accurate molecular crystal nucleation rates at moderate undercooling and, thus, for a high free energy barrier, without influence due to the choice of the progress variable, and without relying on assumptions other than the force field.

A previous estimate found almost 120 orders of magnitude lower rate under nearby conditions,<sup>28</sup> which essentially ruled out the presence of homogeneous nucleation due to the very high free energy barrier obtained. It is likely that most of this discrepancy can be explained by differences in the system setup. Especially, the higher observed solubility of methane under the increased Laplace pressure helps in lowering the barrier and increasing the rate. However, this correction might not be sufficient to explain the discrepancy entirely, and future research might look into examining the rate for a flat methane gas interface using TIS. As this would require a much larger system size, this is beyond the scope of the current work.

Finally, we stress that heterogeneous nucleation can also reduce the free energy barrier of transformation, leading to a faster formation process. A natural extension of this project will be to estimate the rate in a system with heterogeneity.<sup>74</sup>

## ■ ASSOCIATED CONTENT

### SI Supporting Information

The Supporting Information is available free of charge at <https://pubs.acs.org/doi/10.1021/acs.jpbc.0c04582>.

Supporting information text contains information about the system setup, the Gaussian shooting algorithm, avoiding a cylindrical gas reservoir, the effect of small system size, details about RETIS, various plots showing sampling at each interface, the crystallinity of the nucleus, computation of the error in the rate and flux, computation of the free energy barrier and comparison with other rate calculations and CNT (PDF)

Reactive trajectories of transition from liquid phase to solid sI hydrate phase (MCG value of 2–300 in terms of TIS) sampled from the ensemble belonging to interface MCG = 100;  $5^{12}6^2$  and  $5^{12}$  are tracked using blue and red color, respectively. Video 1 (MP4)

Video 2 (MP4)

## ■ AUTHOR INFORMATION

### Corresponding Author

P. G. Bolhuis – van 't Hoff Institute for Molecular Sciences, University of Amsterdam, 1090 GD Amsterdam, The Netherlands; [orcid.org/0000-0002-3698-9258](https://orcid.org/0000-0002-3698-9258); Email: [p.g.bolhuis@uva.nl](mailto:p.g.bolhuis@uva.nl)

### Author

A. Arjun – van 't Hoff Institute for Molecular Sciences, University of Amsterdam, 1090 GD Amsterdam, The Netherlands; [orcid.org/0000-0002-6831-6621](https://orcid.org/0000-0002-6831-6621)

Complete contact information is available at: <https://pubs.acs.org/doi/10.1021/acs.jpbc.0c04582>

### Notes

The authors declare no competing financial interest.

## ■ ACKNOWLEDGMENTS

A.A. and P.G.B. acknowledge funding from the Industrial Partnership Program “Computational Sciences for Energy Research” (Grant no. 15CSER051) of the Foundation for Fundamental Research on Matter (FOM), which is part of the Netherlands Organization for Scientific Research (NWO). This research program is co-financed by Shell Global Solutions International B.V. Both authors thank David W. H. Swenson and Gyorgy Hantal for critically reading the manuscript. The authors acknowledge support from the Nederlandse Organisatie voor Wetenschappelijk Onderzoek (NWO) for the use of supercomputer facilities.

## ■ REFERENCES

- (1) Chandler, D. Interfaces and the driving force of hydrophobic assembly. *Nature* **2005**, *437*, 640–647.
- (2) Walsh, M. R.; Koh, C. A.; Sloan, E. D.; Sum, A. K.; Wu, D. T. Microsecond simulations of spontaneous methane hydrate nucleation and growth. *Science* **2009**, *326*, 1095–1098.
- (3) Klauda, J. B.; Sandler, S. I. Global distribution of methane hydrate in ocean sediment. *Energy Fuels* **2005**, *19*, 459–470.
- (4) Sloan, E. D., Jr. Fundamental principles and applications of natural gas hydrates. *Nature* **2003**, *426*, 353.
- (5) Sloan, E. D., Jr.; Koh, C. *Clathrate Hydrates of Natural Gases*; CRC Press, 2007.
- (6) Kvenvolden, K. A. Potential effects of gas hydrate on human welfare. *Proc. Natl. Acad. Sci. U.S.A.* **1999**, *96*, 3420–3426.
- (7) McElwain, J. C.; Wade-Murphy, J.; Hesselbo, S. P. Changes in carbon dioxide during an oceanic anoxic event linked to intrusion into Gondwana coals. *Nature* **2005**, *435*, 479.
- (8) Koh, C. A.; Sloan, E. D.; Sum, A. K.; Wu, D. T. Fundamentals and applications of gas hydrates. *Annu. Rev. Chem. Biomol. Eng.* **2011**, *2*, No. 237.
- (9) Sosso, G. C.; Chen, J.; Cox, S. J.; Fitzner, M.; Pedevilla, P.; Zen, A.; Michaelides, A. Crystal nucleation in liquids: Open questions and future challenges in molecular dynamics simulations. *Chem. Rev.* **2016**, *116*, 7078–7116.
- (10) Becker, R.; Döring, W. Kinetische behandlung der keimbildung in übersättigten dämpfen. *Ann. Phys.* **1935**, *416*, 719–752.
- (11) Warrior, P.; Khan, M. N.; Srivastava, V.; Maupin, C. M.; Koh, C. A. Overview: Nucleation of clathrate hydrates. *J. Chem. Phys.* **2016**, *145*, No. 211705.
- (12) Schreiber, R. E.; Houben, L.; Wolf, S. G.; Leitun, G.; Lang, Z.-L.; Carbó, J. J.; Poblet, J. M.; Neumann, R. Real-time molecular scale observation of crystal formation. *Nat. Chem.* **2017**, *9*, 369.
- (13) Zhou, J.; Yang, Y.; Yang, Y.; Kim, D. S.; Yuan, A.; Tian, X.; Ophus, C.; Sun, F.; Schmid, A. K.; Nathanson, M.; et al. Observing crystal nucleation in four dimensions using atomic electron tomography. *Nature* **2019**, *570*, 500–503.
- (14) Hall, K. W.; Carpendale, S.; Kusalik, P. G. Evidence from mixed hydrate nucleation for a funnel model of crystallization. *Proc. Natl. Acad. Sci. U.S.A.* **2016**, *113*, 12041–12046.
- (15) Jacobson, L. C.; Hujo, W.; Molinero, V. Amorphous precursors in the nucleation of clathrate hydrates. *J. Am. Chem. Soc.* **2010**, *132*, 11806–11811.
- (16) Jiménez-Ángeles, F.; Firoozabadi, A. Nucleation of methane hydrates at moderate subcooling by molecular dynamics simulations. *J. Phys. Chem. C* **2014**, *118*, 11310–11318.
- (17) Bi, Y.; Li, T. Probing methane hydrate nucleation through the forward flux sampling method. *J. Phys. Chem. B* **2014**, *118*, 13324–13332.
- (18) DeFever, R. S.; Sarupria, S. Nucleation mechanism of clathrate hydrates of water-soluble guest molecules. *J. Chem. Phys.* **2017**, *147*, No. 204503.
- (19) Zhang, Z.; Liu, C.-J.; Walsh, M. R.; Guo, G.-J. Effects of ensembles on methane hydrate nucleation kinetics. *Phys. Chem. Chem. Phys.* **2016**, *18*, 15602–15608.

- (20) Walsh, M. R.; Beckham, G. T.; Koh, C. A.; Sloan, E. D.; Wu, D. T.; Sum, A. K. Methane hydrate nucleation rates from molecular dynamics simulations: effects of aqueous methane concentration, interfacial curvature, and system size. *J. Phys. Chem. C* **2011**, *115*, 21241–21248.
- (21) Yuhara, D.; Barnes, B. C.; Suh, D.; Knott, B. C.; Beckham, G. T.; Yasuoka, K.; Wu, D. T.; Sum, A. K. Nucleation rate analysis of methane hydrate from molecular dynamics simulations. *Faraday Discuss.* **2015**, *179*, 463–474.
- (22) Barnes, B. C.; Knott, B. C.; Beckham, G. T.; Wu, D. T.; Sum, A. K. Reaction coordinate of incipient methane clathrate hydrate nucleation. *J. Phys. Chem. B* **2014**, *118*, 13236–13243.
- (23) Smeets, P. J.; Finney, A. R.; Habraken, W. J.; Nudelman, F.; Friedrich, H.; Laven, J.; De Yoreo, J. J.; Rodger, P. M.; Sommerdijk, N. A. A classical view on nonclassical nucleation. *Proc. Natl. Acad. Sci. U.S.A.* **2017**, *114*, No. 201700342.
- (24) Ostwald, W. Studies on formation and transformation of solid materials. *Z. Phys. Chem* **1897**, *22*, 289–330.
- (25) Bi, Y.; Porras, A.; Li, T. Free energy landscape and molecular pathways of gas hydrate nucleation. *J. Chem. Phys.* **2016**, *145*, No. 211909.
- (26) Lauricella, M.; Meloni, S.; English, N. J.; Peters, B.; Ciccotti, G. Methane clathrate hydrate nucleation mechanism by advanced molecular simulations. *J. Phys. Chem. C* **2014**, *118*, 22847–22857.
- (27) Molinero, V.; Moore, E. B. Water modeled as an intermediate element between carbon and silicon. *J. Phys. Chem. B* **2009**, *113*, 4008–4016.
- (28) Knott, B. C.; Molinero, V.; Doherty, M. F.; Peters, B. Homogeneous nucleation of methane hydrates: Unrealistic under realistic conditions. *J. Am. Chem. Soc.* **2012**, *134*, 19544–19547.
- (29) Thoutam, P.; Rezaei Gomari, S.; Ahmad, F.; Islam, M. Comparative Analysis of Hydrate Nucleation for Methane and Carbon Dioxide. *Molecules* **2019**, *24*, 1055.
- (30) Abay, H. K.; Svartaas, T. M. Multicomponent gas hydrate nucleation: the effect of the cooling rate and composition. *Energy Fuels* **2011**, *25*, 42–51.
- (31) Herri, J.-M.; Pic, J.-S.; Gruy, F.; Cournil, M. Methane hydrate crystallization mechanism from in-situ particle sizing. *AIChE J.* **1999**, *45*, 590–602.
- (32) Lekvam, K.; Ruoff, P. A reaction kinetic mechanism for methane hydrate formation in liquid water. *J. Am. Chem. Soc.* **1993**, *115*, 8565–8569.
- (33) Devarakonda, S.; Groysman, A.; Myerson, A. S. THF-water hydrate crystallization: an experimental investigation. *J. Cryst. Growth* **1999**, *204*, 525–538.
- (34) Takeya, S.; Hori, A.; Hondoh, T.; Uchida, T. Freezing-memory effect of water on nucleation of CO<sub>2</sub> hydrate crystals. *J. Phys. Chem. B* **2000**, *104*, 4164–4168.
- (35) Jensen, L.; Thomsen, K.; von Solms, N. Propane hydrate nucleation: Experimental investigation and correlation. *Chem. Eng. Sci.* **2008**, *63*, 3069–3080.
- (36) Maeda, N. Nucleation curves of methane hydrate from constant cooling ramp methods. *Fuel* **2018**, *223*, 286–293.
- (37) Maeda, N.; Shen, X.-d. Scaling laws for nucleation rates of gas hydrate. *Fuel* **2019**, *253*, 1597–1604.
- (38) Zimmermann, N. E. R.; Vorselaars, B.; Espinosa, J. R.; Quigley, D.; Smith, W. R.; Sanz, E.; Vega, C.; Peters, B. NaCl nucleation from brine in seeded simulations: Sources of uncertainty in rate estimates. *J. Chem. Phys.* **2018**, *148*, No. 222838.
- (39) Bolhuis, P. G.; Chandler, D.; Dellago, C.; Geissler, P. L. Transition path sampling: Throwing ropes over rough mountain passes, in the dark. *Annu. Rev. Phys. Chem.* **2002**, *53*, 291–318.
- (40) van Erp, T. S.; Moroni, D.; Bolhuis, P. G. A novel path sampling method for the calculation of rate constants. *J. Chem. Phys.* **2003**, *118*, 7762–7774.
- (41) Zhang, P.; Wu, Q.; Mu, C. Influence of temperature on methane hydrate formation. *Sci. Rep.* **2017**, *7*, No. 7904.
- (42) Abascal, J.; Sanz, E.; García Fernández, R.; Vega, C. A potential model for the study of ices and amorphous water: TIP4P/Ice. *J. Chem. Phys.* **2005**, *122*, No. 234511.
- (43) Arjun; Berendsen, T. A.; Bolhuis, P. G. Unbiased atomistic insight in the competing nucleation mechanisms of methane hydrates. *Proc. Natl. Acad. Sci. U.S.A.* **2019**, *116*, 19305–19310.
- (44) Conde, M.; Vega, C. Determining the three-phase coexistence line in methane hydrates using computer simulations. *J. Chem. Phys.* **2010**, *133*, No. 064507.
- (45) Moroni, D.; Ten Wolde, P. R.; Bolhuis, P. G. Interplay between structure and size in a critical crystal nucleus. *Phys. Rev. Lett.* **2005**, *94*, No. 235703.
- (46) Lechner, W.; Dellago, C.; Bolhuis, P. G. Role of the prestructured surface cloud in crystal nucleation. *Phys. Rev. Lett.* **2011**, *106*, No. 085701.
- (47) Díaz Leines, G.; Drautz, R.; Rogal, J. Atomistic insight into the non-classical nucleation mechanism during solidification in Ni. *J. Chem. Phys.* **2017**, *146*, No. 154702.
- (48) Haji-Akbari, A.; Debenedetti, P. G. Direct calculation of ice homogeneous nucleation rate for a molecular model of water. *Proc. Natl. Acad. Sci. U.S.A.* **2015**, *112*, 10582–10588.
- (49) van Erp, T. S.; Moroni, D.; Bolhuis, P. G. A Novel Path Sampling Method for the Calculation of Rate Constants. *J. Chem. Phys.* **2003**, *118*, 7762–7774.
- (50) Bolhuis, P. G.; Chandler, D.; Dellago, C.; Geissler, P. L. Transition path sampling: Throwing ropes over rough mountain passes, in the dark. *Annu. Rev. Phys. Chem.* **2002**, *53*, 291–318.
- (51) Bolhuis, P. G.; Dellago, C. *Reviews in Computational Chemistry Inc.*; John Wiley & Sons, Inc.: 2010; pp 111–210.
- (52) Swenson, D. W. H.; Prinz, J.-H.; Noe, F.; Chodera, J. D.; Bolhuis, P. G. OpenPathSampling: A Python Framework for Path Sampling Simulations. 1. Basics. *J. Chem. Theory Comput.* **2019**, *15*, 813–836.
- (53) Swenson, D. W.; Prinz, J.-H.; Noe, F.; Chodera, J. D.; Bolhuis, P. G. OpenPathSampling: A Python Framework for Path Sampling Simulations. 2. Building and Customizing Path Ensembles and Sample Schemes. *J. Chem. Theory Comput.* **2019**, *15*, 837–856.
- (54) van Erp, T. S. Reaction Rate Calculation by Parallel Path Swapping. *Phys. Rev. Lett.* **2007**, *98*, No. 268301.
- (55) Bolhuis, P. G. Rare events via multiple reaction channels sampled by path replica exchange. *J. Chem. Phys.* **2008**, *129*, No. 114108.
- (56) Cabriolu, R.; Refsnes, K. M. S.; Bolhuis, P. G.; van Erp, T. S. Foundations and latest advances in replica exchange transition interface sampling. *J. Chem. Phys.* **2017**, *147*, No. 152722.
- (57) Abascal, J.; Sanz, E.; García Fernández, R.; Vega, C. A potential model for the study of ices and amorphous water: TIP4P/Ice. *J. Chem. Phys.* **2005**, *122*, No. 234511.
- (58) Eastman, P.; Swails, J.; Chodera, J. D.; McGibbon, R. T.; Zhao, Y.; Beauchamp, K. A.; Wang, L.-P.; Simmonett, A. C.; Harrigan, M. P.; Stern, C. D.; et al. OpenMM 7: Rapid development of high performance algorithms for molecular dynamics. *PLoS Comput. Biol.* **2017**, *13*, No. e1005659.
- (59) Sivak, D. A.; Chodera, J. D.; Crooks, G. E. Time step rescaling recovers continuous-time dynamical properties for discrete-time Langevin integration of nonequilibrium systems. *J. Phys. Chem. B* **2014**, *118*, 6466–6474.
- (60) Barnes, B. C.; Beckham, G. T.; Wu, D. T.; Sum, A. K. Two-component order parameter for quantifying clathrate hydrate nucleation and growth. *J. Chem. Phys.* **2014**, *140*, No. 164506.
- (61) Jacobson, L. C.; Hujo, W.; Molinero, V. Thermodynamic stability and growth of guest-free clathrate hydrates: a low-density crystal phase of water. *J. Phys. Chem. B* **2009**, *113*, 10298–10307.
- (62) Zhang, Z.; Walsh, M. R.; Guo, G.-J. Microcanonical molecular simulations of methane hydrate nucleation and growth: evidence that direct nucleation to sI hydrate is among the multiple nucleation pathways. *Phys. Chem. Chem. Phys.* **2015**, *17*, 8870–8876.

(63) Sarupria, S.; Debenedetti, P. G. Homogeneous nucleation of methane hydrate in microsecond molecular dynamics simulations. *J. Phys. Chem. Lett.* **2012**, *3*, 2942–2947.

(64) Haji-Akbari, A. Forward-flux sampling with jumpy order parameters. *J. Chem. Phys.* **2018**, *149*, No. 072303.

(65) Kumar, S.; Rosenberg, J. M.; Bouzida, D.; Swendsen, R. H.; Kollman, P. A. The weighted histogram analysis method for free-energy calculations on biomolecules. I. The method. *J. Comput. Chem.* **1992**, *13*, 1011–1021.

(66) Swenson, D. W. H.; Bolhuis, P. G. A replica exchange transition interface sampling method with multiple interface sets for investigating networks of rare events. *J. Chem. Phys.* **2014**, *141*, No. 044101.

(67) Rogal, J.; Lechner, W.; Juraszek, J.; Ensing, B.; Bolhuis, P. G. The reweighted path ensemble. *J. Chem. Phys.* **2010**, *133*, No. 174109.

(68) Newton, A. C.; Groenewold, J.; Kegel, W. K.; Bolhuis, P. G. Rotational diffusion affects the dynamical self-assembly pathways of patchy particles. *Proc Natl. Acad. Sci. U.S.A.* **2015**, *112*, 15308–15313.

(69) Jacobson, L. C.; Molinero, V. Can amorphous nuclei grow crystalline clathrates? The size and crystallinity of critical clathrate nuclei. *J. Am. Chem. Soc.* **2011**, *133*, 6458–6463.

(70) Anderson, R.; Llamedo, M.; Tohidi, B.; Burgass, R. W. Experimental measurement of methane and carbon dioxide clathrate hydrate equilibria in mesoporous silica. *J. Phys. Chem. B* **2003**, *107*, 3507–3514.

(71) Kashchiev, D.; Firoozabadi, A. Driving force for crystallization of gas hydrates. *J. Cryst. Growth* **2002**, *241*, 220–230.

(72) Juraszek, J.; Bolhuis, P. G. Rate constant and reaction coordinate of Trp-cage folding in explicit water. *Biophys. J.* **2008**, *95*, 4246–4257.

(73) Van Erp, T. S. Dynamical rare event simulation techniques for equilibrium and nonequilibrium systems. *Adv. Chem. Phys.* **2012**, *151*, No. 27.

(74) Cox, S. J.; Taylor, D. J.; Youngs, T. G.; Soper, A. K.; Totton, T. S.; Chapman, R. G.; Arjmandi, M.; Hodges, M. G.; Skipper, N. T.; Michaelides, A. Formation of methane hydrate in the presence of natural and synthetic nanoparticles. *J. Am. Chem. Soc.* **2018**, *140*, 3277–3284.